Check for updates

David A. Steinman[1]
e-mail: steinman@mie.utoronto.ca

Yiemeng Hoi

University of Toronto,
Toronto, ON, M5S 3G8 Canada

Paul Fahy

Liam Morris

Galway Mayo Institute of Technology,
Galway, Ireland

Michael T. Walsh
University of Limerick,
Limerick, Ireland

Nicolas Aristokleous

Andreas S. Anayiotos

Cyprus University of Technology,
Limassol, 3036 Cyprus

Yannis Papaharilaou
Foundation for Research and Technology–Hellas,
Heraklion, 71110 Greece

Amirhossein Arzani

Shawn C. Shadden

Illinois Institute of Technology,
Chicago, IL, 60616

Philipp Berg

Gábor Janiga

Otto von Guericke University of Magdeburg,
Magdeburg, 39106 Germany

Joris Bols

Patrick Segers

Ghent University,
9000 Ghent, Belgium

Neil W. Bressloff
University of Southampton,
Southampton, Hampshire, SO17 1BJ UK

Merih Cibis

Frank H. Gijsen

Erasmus MC,
Rotterdam, Netherlands

Salvatore Cito

Jordi Pallarés

University Rovira i Virgili,
Tarragona, Catalonia, 43007 Spain

Leonard D. Browne

Variability of Computational Fluid Dynamics Solutions for Pressure and Flow in a Giant Aneurysm: The ASME 2012 Summer Bioengineering Conference CFD Challenge

Stimulated by a recent controversy regarding pressure drops predicted in a giant aneurysm with a proximal stenosis, the present study sought to assess variability in the prediction of pressures and flow by a wide variety of research groups. In phase I, lumen geometry, flow rates, and fluid properties were specified, leaving each research group to choose their solver, discretization, and solution strategies. Variability was assessed by having each group interpolate their results onto a standardized mesh and centerline. For phase II, a physical model of the geometry was constructed, from which pressure and flow rates were measured. Groups repeated their simulations using a geometry reconstructed from a micro-computed tomography (CT) scan of the physical model with the measured flow rates and fluid properties. Phase I results from 25 groups demonstrated remarkable consistency in the pressure patterns, with the majority predicting peak systolic pressure drops within 8% of each other. Aneurysm sac flow patterns were more variable with only a few groups reporting peak systolic flow instabilities owing to their use of high temporal resolutions. Variability for phase II was comparable, and the median predicted pressure drops were within a few millimeters of mercury of the measured values but only after accounting for submillimeter errors in the reconstruction of the life-sized flow model from micro-CT. In summary, pressure can be predicted with consistency by CFD across a wide range of solvers and solution strategies, but this may not hold true for specific flow patterns or derived quantities. Future challenges are needed and should focus on hemodynamic quantities thought to be of clinical interest. [DOI: 10.1115/1.4023382]

Downloaded from asmedigitalcollection.asme.org/biomechanical/article-pdf/135/2/021016/6088427/bio_135_2_021016.pdf by Tufts University user on 15 November 2026

[1]Corresponding author.

Contributed by the Bioengineering Division of ASME for publication in the JOURNAL OF BIOMECHANICAL ENGINEERING. Manuscript received November 7, 2012; final manuscript received December 22, 2012; accepted manuscript posted January 18, 2013; published online February 11, 2013. Editor: Victor H. Barocas.

Jennifer A. Costelloe

Adrian G. Lynch

University of Limerick,
Limerick, Ireland

Joris Degroote

Jan Vierendeels

Ghent University,
Ghent, 9000 Belgium

Wenyu Fu

Aike Qiao

Beijing University of Technology,
Beijing, 100124 China

Simona Hodis

David F. Kallmes

Mayo Clinic,
Rochester, MN, 55905

Hardeep Kalsi

Quan Long

Brunel University,
London, UB8 3PH UK

Vitaly O. Kheyfets

Ender A. Finol

University of Texas at San Antonio,
San Antonio, TX, 78229

Kenichi Kono
Wakayama Rosai Hospital,
Wakayama, 640-8505 Japan

Adel M. Malek

Alexandra Lauric

Tufts Medical Center,
Boston, MA 02111

Prahlad G. Menon

Kerem Pekkan

Carnegie Mellon University,
Pittsburgh, PA 15219

Mahdi Esmaily Moghadam

Alison L. Marsden

University of California San Diego,
San Diego, CA 92093

Marie Oshima
The University of Tokyo,
Tokyo, 153-8505 Japan

Kengo Katagiri
Shibaura Institute of Technology,
Tokyo, 135-8548 Japan

Véronique Peiffer

Yumnah Mohamied

Spencer J. Sherwin

Imperial College London,
London, SW7 2AZ UK

Jens Schaller

Leonid Goubergrits

Charite-Universitatsmedizin Berlin,
Berlin, 14195 Germany

Gabriel Usera

Mariana Mendina

Universidad de la Republica,
Montevideo, 11300 Uruguay

Kristian Valen-Sendstad

Damiaan F. Habets

University of Toronto,
Toronto, ON, M5S 3G8 Canada

Jianping Xiang

Hui Meng

State University of New York at Buffalo,
Buffalo, NY 14203

Yue Yu

George E. Karniadakis

Brown University,
Providence, RI 02912

Nicholas Shaffer

Francis Loth

University of Akron,
Akron, OH 44325

Introduction

Image-based computational fluid dynamics (CFD) has emerged in the past decade as a powerful and popular tool for the study of blood flow dynamics and their role in the development, diagnosis, and treatment of cardiovascular disease [1]. The essential ingredients in any image-based CFD model are the lumen geometry, often derived from 3D angiography, and the inlet and outlet flow rates, often assumed although occasionally based on patient-specific measurements. The sensitivity of image-based CFD to these and to the various modeling assumptions and uncertainties has been investigated thoroughly. Generally speaking, uncertainty in the lumen geometry, typically owing to the segmentation method but also due to the choice of imaging modality/resolution, tends to introduce the greatest variability into the CFD solutions. For large artery flows at least, rigid walls, Newtonian viscosity, and fully developed inflow assumptions are generally thought to have a second-order effect [2]. Numerous individual studies have also been carried out to validate image-based CFD predictions against careful *in vitro* measurements (e.g., Refs. [3–5]) or

Downloaded from asmedigitalcollection.asme.org/biomechanical/article-pdf/135/2/021016/6088427/bio_135_2_021016.pdf by Tufts University user on 15 November 2026

available *in vivo* data (e.g., Refs. [6–8]); however, few studies in the biofluids literature have evaluated the sensitivity of CFD predictions to different solvers or groups. Notable exceptions have been the Virtual Intracranial Stent Challenges [9] and the FDA nozzle benchmark [10].

For several years, authors Steinman and Loth aimed to lead an image-based CFD Challenge to compare solutions contributed by different groups, but hesitated for lack of a problem for which the hemodynamic quantities, and hence their variability, could be put in the context of their clinical utility. This was effectively remedied by a recent controversy in the neuroradiology literature, which provided an ideal problem to test. In 2010, Cebral et al. [11] proposed a possible explanation for the rupture of giant cerebral aneurysms that had been observed following deployment of flow-diverting stents. Their hypothesis was that deployment of the flow diverter might lead to a relief or redistribution of pressure drops along the parent artery and cause a posttreatment rise in aneurysm sac pressure. This was demonstrated in three cases, for which 20–25 mmHg increases in pressure were predicted by comparing pre- and posttreatment CFD models.

Soon after the Cebral et al. publication [11], Fiorella et al. [12] wrote a letter to the editor questioning the pretreatment pressure drops (and, hence, posttreatment pressure rises) as unphysiologically high, citing basic fluid mechanics theory and animal experiments. A number of potential culprits were suggested for this overestimation of pressure, including the presumed flow rates, the assumption of a rigid wall, and the CFD solver itself. In their response, Cebral et al. argued that their CFD solver had been validated against *in vitro* measurements of pressure drops across a stenosis [13] and that, although the flow rates were assumed and not patient-specific, they were plausible. In a commentary commissioned by the journal, Steinman [14] concluded that the pressures may be overestimated, albeit to an uncertain extent, and that the culprit was likely the assumed flow rates rather than compliance effects or CFD solver errors. In light of the specific concerns expressed by Fiorella et al. [12] about the CFD solution itself, we thought it was important to conduct a CFD Challenge that would document the variability of many different CFD groups that used a variety of solvers. We elected to choose one case from Ref. [11] as being sufficiently challenging in terms of the geometry—a giant aneurysm with a tortuous parent artery having a constriction proximal to the aneurysm—and of obvious clinical interest.

The primary objective of this CFD Challenge was to determine the "real world" variability of CFD solutions in a case where all participants were provided with the same lumen geometry and flow rate boundary conditions, but were given no guidance regarding solution strategy, discretization, etc. A secondary objective was to confirm or refute the pressure drops predicted by Cebral et al. [11] for their choice of flow rates. It must be emphasized here that our objective was decidedly *not* to test Cebral et al.'s clinical hypothesis; however, in light of concerns about the assumed flow rates, we felt it was important to incorporate additional flow rates into the Challenge so as to determine how sensitive the results are to that key assumption.

Methods

The stages and timelines for the CFD Challenge are summarized in Table 1. Briefly, the Challenge consisted of two phases: phase I, testing the variability of the contributed solutions and phase II, comparing the predicted pressure drops to those measured in a physical model of the same geometry. Participants were invited to submit an abstract to the ASME 2012 Summer Bioengineering Conference (SBC2012), outlining their methods and presenting their preliminary phase I results. Groups whose abstracts were accepted were then invited to submit complete phase I and II solutions for presentation at a workshop at SBC2012.

Table 1 Timeline for SBC2012 CFD Challenge

Phase	Date/Deadline
Phase I announced	September 6, 2011
Abstract guidelines sent	December 6, 2011
SBC2012 abstract deadline	January 15, 2012
Phase II announced	April 22, 2012
Data submission guidelines sent	May 12, 2012
Data submission deadline	June 15, 2012
SBC2012 workshop	June 21, 2012

Participants and Solution Strategies. In total, 28 abstracts were submitted to SBC2012, comprising 31 different solutions. One abstract/solution was withdrawn before review, and one was rejected for incomplete data. Of the abstracts accepted for SBC2012, 27 complete solutions were ultimately submitted for phase I and 24 for phase II.

Of the 25 different groups that contributed complete Phase I solutions, 12 were based in Europe, 9 in North America, 3 in Asia, and 1 in South America. Of the 27 phase I solutions, 17 used commercial solvers (11 Fluent, 2 CFX, 2 Star-CCM+, 1 Star-CD, 1 FIDAP), 5 were based on open-source platforms (two Nektar and one each for caffa3D.MB, FEnICS, and OpenFOAM), and 5 used in-house solvers. The majority of solutions were based on the finite volume method (19), with five finite element, two spectral element, and one finite difference. The majority (19) also employed tetrahedra-dominant meshes, followed by five hexahedra-dominant, two polyhedral meshes, and two uniformly spaced Cartesian grids with immersed boundaries. Three solutions also used some kind of two-equation turbulence modeling.

Owing to the wide variety of element types, solution orders, and meshing strategies (e.g., use of flow extensions, boundary layer meshes, nonuniform spacing, etc.), it was difficult to standardize the comparison in terms of elements, nodes, or degrees-of-freedom. Instead, participants were asked to report the nominal spatial resolution for the phase I, pulsatile2 case. The median was 0.18 mm, and half the solutions were between 0.15 mm and 0.26 mm (i.e., defining the interquartile range, IQR). The finest meshes were 0.1 mm, and the coarsest 1.0 mm, although in the latter case finer boundary layer elements were used. The median temporal resolution was 1.0 ms (~1000 steps/cycle), with an interquartile range of 0.17 ms to 4 ms (234 steps/cycle to 6000 steps/cycle). At the extremes were solutions with 0.46 μs (2.2×10^6 steps/cycle) and 5 ms (198 steps/cycle).

Finally, although inlet flow rates were prescribed, as described below, participants were free to choose inlet velocity boundary conditions most convenient to their solver, and with flow extensions as needed or desired. Just over half the solutions reported imposing fully developed velocities (seven Poiseuille, eight Womersley) and the rest (12) used uniform/plug. Participants were similarly free to prescribe suitable outlet conditions, although in most cases a standard traction free condition was sufficient in light of the single outlet.

Phase I

Lumen Geometry. The case selected from Ref. [11] was that of patient #1, who had a giant cerebral aneurysm with a constriction proximal to the aneurysm ostium. A surface mesh corresponding to the pretreatment lumen geometry of patient #1 was generously provided by Juan Cebral. The original mesh of ~81,000 triangles was doubled in resolution to 3.25×10^5 triangles using the Vascular Modeling ToolKit's (VMTK [15]) surface subdivision with a butterfly option, in order to accommodate participants who might be using finer volume meshes. The surface mesh, shown in Fig. 1, was provided to Challenge participants in ASCII STL format.

VMTK was used to automatically compute the centerline and cross-sectional areas. It was determined that the minimum cross-

Downloaded from asmedigitalcollection.asme.org/biomechanical/article-pdf/135/2/021016/6088427/bio_135_2_021016.pdf by Tufts University user on 15 November 2026

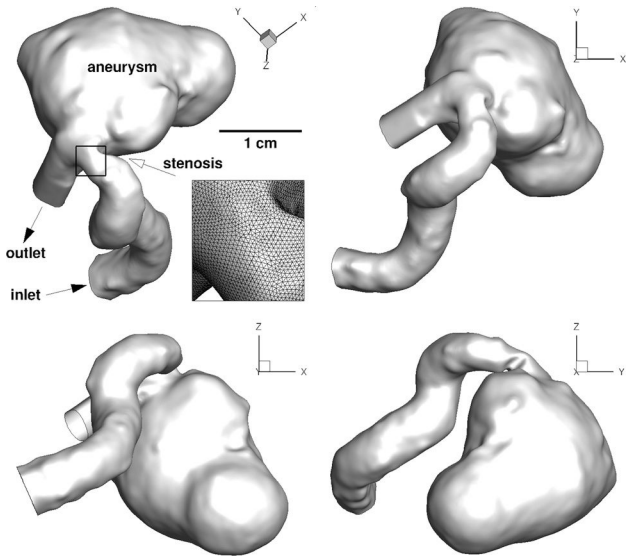


Fig. 1 Phase I CFD model geometry. Top left panel shows an isometric overview of the model, with scale bar indicating size and inset indicating density of surface triangulation provided to Challenge participants. The remaining three panels show the geometry viewed along each of the cardinal axes.

sectional area of the stenosis was 7.49 mm^2. Relative to the nominal inlet area of 24.45 mm^2, this corresponds to an area reduction of 69% or a diameter reduction of 45% assuming a circular cross section.

Flow Conditions. Pulsatile flow boundary conditions were based on a flow rate waveform again provided by Juan Cebral. The flow waveform had a period of 0.99 s, and data were provided at a regular interval of 0.01 s. These data were Fourier-decomposed up to the first 22 harmonics, which were provided to the Challenge participants so as to allow them to prescribe consistent flow rate boundary conditions at any temporal resolution. The resulting waveform, shown in Fig. 2, had a mean flow rate of 6.41 mL/s, based on Cebral et al.'s [11] assumption of an inlet cycle-averaged wall shear stress (WSS) of 15 dyn/cm^2, an assumed Newtonian blood viscosity of 0.04 Poise, and the nominal inlet diameter of 5.58 mm. The corresponding peak flow rate was 11.42 mL/s. A blood density of 1.0 g/cm^3 was also assumed by Cebral et al., resulting in cycle-averaged and peak Reynolds numbers of 366 and 651, respectively, and a Womersley number of 3.48.

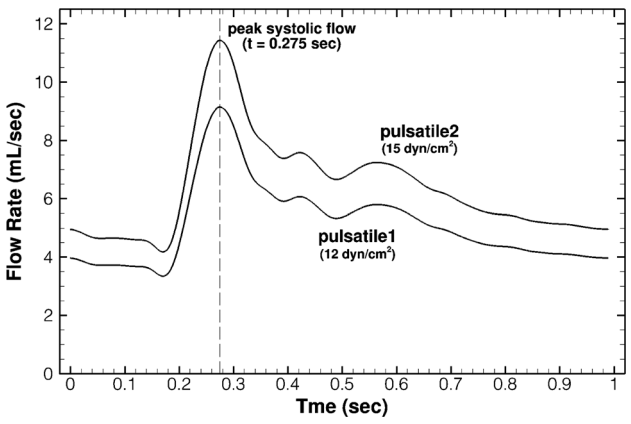


Fig. 2 Phase I pulsatile flow rates. Both flow waveforms have identical shapes, with means derived from the nominal cycle-averaged inlet WSS indicated, as described in the Methods.

Table 2 Prescribed fluid and flow parameters for phase I and II CFD studies

	Phase I	Phase II
Viscosity (dyn-s/cm^2)	0.04	0.0401
Density (g/cm^3)	1.000	1.113
Period (s)	0.99	1.164
Flow rates (mL/s)		
AV1 (SS1)	5.13 (5.13)	4.40 (5.10)
AV2 (SS2)	6.41 (6.41)	6.16 (6.36)
PK1 (SS3)	9.14 (9.14)	9.34 (9.17)
PK2 (SS4)	11.42 (11.42)	11.25 (11.36)

Given the concerns expressed about how the choice of flow rate might affect the pressure drop, another pulsatile flow case was defined identically to the first, except based on an inlet cycle-averaged WSS of 12 dyn/cm^2. This value was chosen for two reasons: first, it is roughly in the middle of the typical range of cycle-averaged WSS for the carotid artery [16]; and second, as noted below and shown in Table 2, it provides a more uniform sequence of flow rates for complementary steady flow studies. This lower WSS-based waveform will be referred to as *pulsatile1*, and the higher WSS-based waveform will be referred to as *pulsatile2*, per Fig. 2. We will refer to the cycle-averaged and peak-systolic conditions for these two flow waveforms as AV1, AV2, PK1, and PK2, per Table 2. Participants were also asked to carry out a separate set of simulations under steady flow rates corresponding to AV1, AV2, PK1, and PK2 conditions. Per Table 2, these are referred to as SS1, SS2, SS3, and SS4. These were requested to test the quasi-steady assumption for pressure and also to assess the variability in predicted pressures in the absence of more complicated pulsatile flow conditions.

Aside from the prescribed flow rates, there were no other constraints imposed on the participants regarding inflow and outflow boundary conditions: Participants could add flow extensions as needed and could choose whichever inlet velocity profile (e.g., plug, Poiseuille, Womersley) they preferred and/or was available for their CFD solver.

Phase II

Model Fabrication. For the experiments it was decided to construct a physical flow model at life size, since we did not intend to resolve flow details and we wanted to ensure adequate dynamic range for the measured pressure drops. Starting from the STL file provided to participants of phase I, inlet and outlet tube extensions were digitally added using Pro/Engineer (Wildfire 4.0, PTC, Needham, MA) to facilitate connecting to an intracranial test system. An acrylonitrile butadiene styrene (ABS) model was manufactured on a rapid prototyping (RP) machine (Prodigy Plus, Stratasys, Frankfurt, Germany) with a slice thickness of 0.0178 mm. The RP surface was smoothed and sealed by repeated dipping in xylene and isopropyl alcohol for 1 min intervals. Tubes were placed over the inlet and outlet and extended several diameters to provide a smooth and leak-free connection to the flow system tubing. The ABS core model was cast in a silicone block (Essil 291, Axson, Paris, France) with a 20% mixture of silicone fluid (Dow Corning, Seneffe, Belgium). This ABS core model was cut out and removed from the silicone mold. This silicone mold was then used to create a new inner core model made from a low melting point alloy (LMPA) (Tiranti, Berkshire, UK), as shown in Fig. 3(*a*). This LMPA core was positioned inside a polycarbonate box with pressure ports incorporated onto the model using 21 gauge needles (Becton Dickson, Franklin Lakes) positioned 26 mm and 24 mm from the stenosis entrance and exit respectively. A third needle was positioned on the aneurysm dome. The rigid flow model was manufactured by pouring a clear polyester resin (Tiranti, Berkshire, UK) into the assembled polycarbonate box and allowed to cure for 24 hr. After curing of the polyester model,

Downloaded from asmedigitalcollection.asme.org/biomechanical/article-pdf/135/2/021016/6088427/bio_135_2_021016.pdf by Tufts University user on 15 November 2026

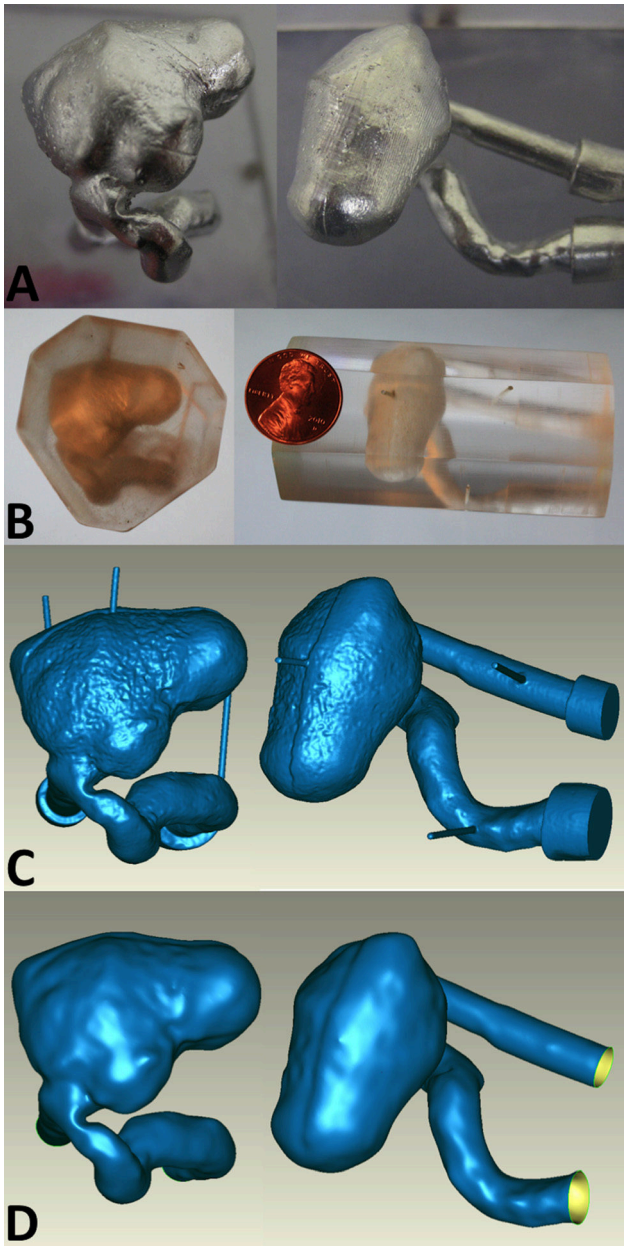


Fig. 3 Physical model construction. (*a*) Low melting point metal alloy inner core. (*b*) Final clear polyester resin aneurysm flow model, with a penny (diameter 19.05 mm) indicating scale of model on the right. (*c*) Surface reconstruction of CT scans of model. (*d*) Final CFD model surface, after pressure port removal, surface smoothing, and end clipping.

the LMPA was melted at 90 °C leaving a hollow core (melting point of LMPA is 70 °C). This method of model construction was similar to techniques previously applied for creating larger arterial models [17–19] and smaller cranial models [20]. The polyester cured with an exothermic reaction and was placed in a cool environment (<0 °C) in order to avoid premelting of the LMPA, thus reducing possible model shrinkage. The finished flow model was cut to size, as shown in Fig. 3(*b*), to be able to fit inside a micro-CT scanner.

Surface Reconstruction. The finished polyester flow model was imaged at the Northeast Ohio Medical University using a micro-CT scanner (VivaCT75, Scanco Medical, Switzerland) with 41 μm resolution. Image quality was mostly good, however, there were large bright spots near the lumen edge at various locations throughout the model, which made segmentation difficult in those regions. The spots were thought to be caused by residual LMPA attached to the plastic lumen wall. Repeated attempts were made to remove the metal using a nitric acid wash (1:9 with de-ionized water), with no improvement, suggesting that the LMPA was actually embedded in the plastic wall. In an attempt to get improved images, the plastic model was subsequently imaged at the Robarts Research Institute in London, Canada using micro-CT (eXplore CT 120, GE Healthcare, London, Canada) with 50 μm resolution. Artifacts were reduced but still evident. The resulting STL surface provided from the scanner software is shown in Fig. 3(*c*). The small surface roughness observed in the reconstruction of the micro-CT was also observed in the flow model (Fig. 3(*a*)); however, these high-frequency surface features were smoothed using VMTK's volume-preserving Taubin filter in order to avoid difficulties in CFD volume mesh generation. The pressure ports were digitally removed and inlet and outlet ends were clipped using Geomagic Studio (Version 11, Geomagic Inc., Morrisville, NC) to produce a smooth representation of the geometry (Fig. 3(*d*)). This is the geometry that was provided, also in ASCII STL format, for phase II of the CFD Challenge.

Fluid Properties. A 54.6:45.4% ratio of de-ionized water to glycerol mixture by weight was used. Multiple viscosity (n = 5) and density (n = 10) measurements were taken before, during, and after testing. The fluid had a viscosity, 4.01 ± 0.04 mPa-s at 26 °C as found from a digital cone and plate viscometer with attached temperature controlled heater bath (DV-II +PRO and TC-102, Brookfield, Essex, UK). The viscometer was calibrated using a viscosity standard fluid, and measurements of the viscosity standard taken before and after the measurement of the working fluid showed the viscometer to have less than 0.5% error. Fluid density was measured to be 1113 ± 3.65 kg/m^3 using a 50 mL burette and a digital scale. These fluid properties were specified for phase II, as summarized in Table 2.

Flow Circuit. A physiological flow system was designed and manufactured at the Galway Medical Technologies Centre (GMedTech), capable of generating steady and unsteady flow conditions into the rigid flow model. A data acquisition card (USB-6009, National Instruments, Berkshire, UK) was used to acquire the input data from the flow and pressure sensors with a sampling rate of 250 Hz. Dedicated software was written in Labview V8.6 (National Instruments, Berkshire, UK) that controlled, monitored, and displayed the pressure and flow rates. Steady flows were simulated using the Iwaki direct drive centrifugal pump (Cole Palmer, Dublin, Ireland). Pulsatile flow was simulated by a computer controlled linear actuator (Aerotech, Southampton, UK) connected to a hydraulic cylinder (SMC, Dublin, Ireland). A clip-on 4PXL ultrasonic probe (Transonic Systems, Maastricht, Netherlands) was used to measure the flow rates. The flow sensor was clamped onto Tygon R-3603 tubing (Cole Palmer, Dublin, Ireland) at the inlet and outlet segments. Three pressure transducers (0 to 260 mmHg range, diaphragm type sensor, Cole Palmer, Dublin, Ireland) connected to 21 gauge needles measured the pressure at the inlet, outlet, and within the aneurysm sac. Compliance downstream of the outlet in the form of a windkessel chamber was used to minimize high pressure spikes, which can occur for rapid flow acceleration in a rigid test system under pulsatile conditions. During testing the fluid temperature was kept constant at 26 °C using two immersion thermostats (GP200, Grant, Cambridge, UK).

Flow Rate Measurements. The ultrasonic flowmeter was calibrated by timed collections. For the pulsatile flow studies, measurements were collected for nine consecutive cycles, and this was repeated three times for each of the two pulsatile cases. As shown in Table 2, the replicated (phase II) peak systolic flow rates were within 2% of the nominal (phase I) values. The cycle-averaged flow rates were somewhat less, owing to the fact that the replicated waveform had a 16% longer period due to the time

Downloaded from asmedigitalcollection.asme.org/biomechanical/article-pdf/135/2/021016/6088427/bio_135_2_021016.pdf by Tufts University user on 15 November 2026

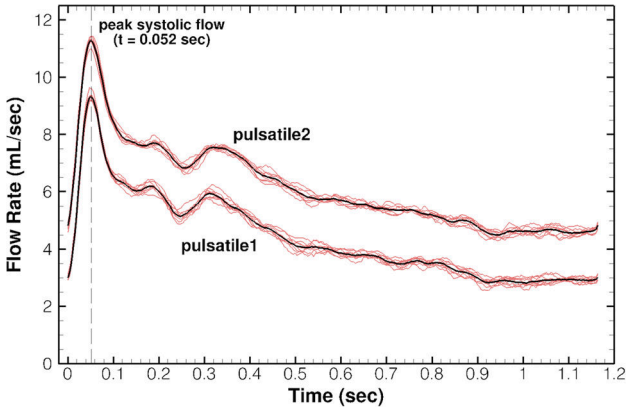


Fig. 4 Phase II measured flow rates. Shown in light red are the nine consecutive cycles superimposed, which were used to determined the respective phase-averaged flow rates (black lines).

required to retract the piston during the refill phase. Flow waveforms for phase II were derived from the measured flow rates by phase-averaging the nine consecutive cycles from the first of the three repeats. The resulting waveforms, shown in Fig. 4, demonstrate the excellent cycle-to-cycle repeatability, which was within $<4\%$ for the peak systolic flow rates, and $<1\%$ for the cycle-averaged flow rates. The resulting flow parameters are summarized in Table 2. Steady flow experiments were repeated six times each. The resulting flow rates were within $<1\%$ of their nominal values and repeatable to within 1%.

Pressure Measurements. Pressure transducers were calibrated with known head heights. The transducers were validated against Poiseuille flow for four flows in a straight rigid PTFE tube of inner diameter 4.8 mm (Cole Palmer, Dublin, Ireland), and agreed to within 3.5%. Pressure measurements from the aneurysm dome were discarded owing to artifacts later attributed to insertion of the transducer tip slightly into the flow field. Inlet and outlet pressures were analyzed similarly to the flow rates, i.e., phase-averaged over nine cycles. Figure 5 shows the individual and phase-averaged inlet and outlet pressures from pulsatile2 run #1, demonstrating excellent repeatability. For pressure drop, the phase-averaged waveform was obtained by taking the difference between the phase-averaged inlet and outlet pressures.

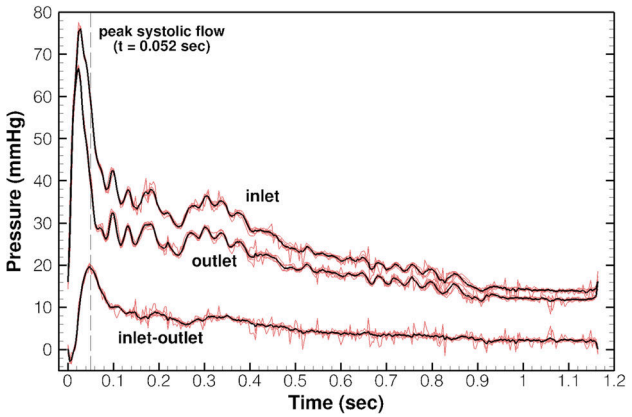


Fig. 5 Phase II measured pressures for pulsatile2 case. Shown are the measured inlet and outlet pressures, and the pressure drop derived from inlet-outlet pressure drop. Shown in red are the nine consecutive cycles superimposed, which were used to determine the respective phase-averaged inlet and outlet pressures, from which the phase-averaged pressure drop was calculated.

CFD Data Analysis. Analysis of data focused on peak systolic and cycle-averaged pressures and velocity magnitudes. The time of peak systole was specified in both cases, as indicated in Fig. 2 and Fig. 4. To facilitate an objective and automated comparison of results, participants were asked to interpolate their data onto a standard volume mesh, surface mesh, or centerline points. Specifically, a linear tetrahedral volume mesh with a nominal node spacing of 0.5 mm was created using VMTK, resulting in $\sim 1.5 \times 10^5$ nodes and $\sim 9 \times 10^5$ elements. This volume mesh was used to visualize velocity magnitude isosurfaces. Surface pressures were visualized on a surface mesh extracted from the volume mesh, consisting of $\sim 1.5 \times 10^4$ nodes and $\sim 3 \times 10^4$ triangles. Surface nodes were projected along their inward-pointing normals by 0.05 mm to ensure intersection with the differently discretized CFD models. A centerline was extracted via VMTK with a 0.25 mm uniform spacing and used to plot centerline velocity magnitudes and pressures, as well as compute inlet-outlet pressure drops.

All data were analyzed centrally at the University of Toronto and visualized and plotted for presentation using Tecplot 360 (Tecplot, Inc., Bellevue WA). Data were contributed prior to the CFD Challenge Workshop, so that participants were not influenced by the final results. To ensure anonymity of the presented results, all contributed solutions were assigned an identification letter known only to the contributing group and the central analysis site. Details about the various groups' solution strategies may be found in the series of CFD Challenge abstracts published in the proceedings of SBC2012; however, to maintain anonymity, only the general characteristics of the solvers are provided here, and they are not linked to the indicated solution IDs. With the permission of the respective two groups, an exception was made for solutions W and X, which were both based on a spectral element solver (Nektar) with high effective spatial and temporal resolution and, thus, were considered closest to a "gold standard."

Results

Phase I—Pressures. As shown in Fig. 6, peak systolic pressures for the higher pulsatile flow case (PK2) agreed well across most solutions, indicating a pressure within the aneurysm sac of around 105 mmHg, which is a pressure drop of 15 mmHg from the inlet. Notable exceptions were solutions H, M, and U, which reported sac pressures closer to 110 mmHg. On the other hand, the solution from Ref. [11], shown at bottom right in Fig. 6, suggests a sac pressure of 100 mmHg or lower. Similarly good overall agreement was seen for the corresponding cycle-averaged pressures (AV2) in Fig. 7, with the exception of solutions M, N, and U. It is also worth noting that the spatial patterns of pressure were broadly similar for PK2 and AV2, irrespective of the absolute pressure levels. Similar trends with regard to agreement and outliers were noted for surface maps of PK1 and AV1 (not shown).

A closer look at the pressure along the centerline is provided in Fig. 8. The major pressure drop occurred around the point of maximum stenosis (axial position $\approx$ 3.8 cm), followed by a small pressure recovery and then a further, more mild, pressure drop past the aneurysm neck (axial position $\approx$ 4.0–4.6 cm). Most solutions showed similar relative trends except for solution E, which predicted a much steeper pressure drop at the stenosis. The degree of pressure recovery distal to the stenosis (axial position $\approx$ 4.0 cm) was variable, with many solutions predicting no pressure recovery at all. Similar results were seen for the four steady flow cases (not shown). Inspection of the rightmost end of the curves (i.e., the outlet at axial position $\approx$ 5.2 cm) in Fig. 8 reveals the range of inlet-outlet pressure drops as predicted by the various solvers. Descriptive statistics provided in Table 3 show that half of the solutions were within less than 1 mmHg of each other, except for PK2, where this interquartile range (IQR) was still only 1.6 mmHg. It is worth noting, however, that the two Nektar solutions differed by around 3 mmHg (19 mmHg versus 22 mmHg) for

Downloaded from asmedigitalcollection.asme.org/biomechanical/article-pdf/135/2/021016/6088427/bio_135_2_021016.pdf by Tufts University user on 15 November 2026

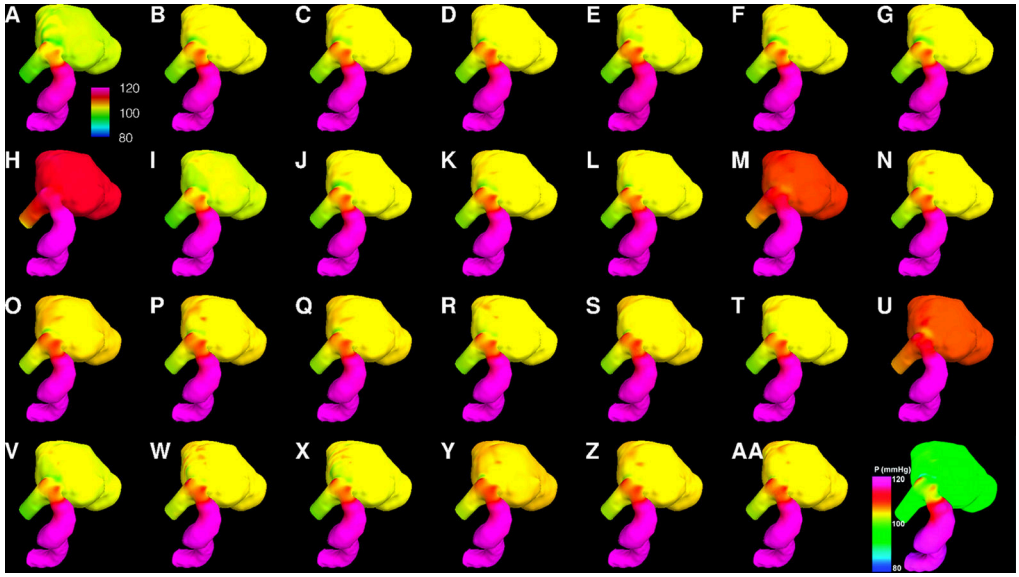


Fig. 6 Surface maps of peak systolic pressures for phase I, pulsatile2 flow (PK2). Letters identify the different contributed solutions, and in all cases are presented with the inlet pressure set to 120 mm Hg and a color scale ranging from 80–120 mm Hg, as shown in panel A. Note the outlier cases H, M, U, as well as the original panel from Ref. [11], bottom right.

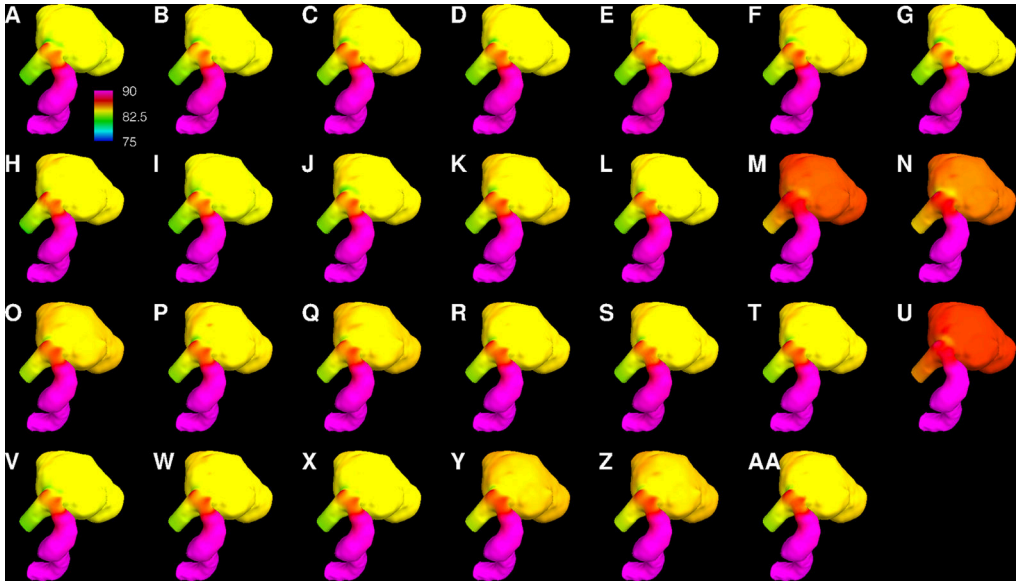


Fig. 7 Surface maps of cycle-averaged pressures for phase I pulsatile2 flow (AV2). Inlet pressure is assumed to be 90 mm Hg, and the color scale now ranges from 75–90 mm Hg. Note the outlier cases M, N, U.

PK2 conditions, whereas they were in near-perfect agreement for PK1, AV2, and AV1. Expressed as a percentage of the median, the IQR was 6–8% for the pulsatile conditions and slightly lower (about 4–7%) for the steady flows. Looking at Table 3, the lower ends of the IQR (i.e., the 25th percentile values) for pulsatile conditions were further from the medians than the upper ends, indicating that solutions tended to underestimate the pressure drops, at least relative to the respective median values.

Plotting the results from Table 3 against the respective flow rates, Fig. 9 reveals that the pressure drops followed the expected nonlinear behavior for both pulsatile and steady conditions ($R^2 > 0.999$). This also highlighted the negligible differences for peak systolic and cycle-averaged pressure drops relative to their steady flow counterparts, suggesting that a quasi-steady approximation would be reasonable.

Phase I—Velocities. Peak systolic velocities for the pulsatile2 case (PK2) shown in Fig. 10 reveal a greater degree of variability among the solutions in terms of sac inflow patterns. For instance, solutions D, H, O, S, and T predicted relatively little penetration of the 50 cm/s velocity isosurface into the sac, whereas several others (e.g., L, N, Z) were comparable to that predicted by Ref. [11]. In some solutions there was also evidence of flow instabilities (e.g., A, R, U, W, X, AA). Common to these was a temporal resolution below 0.2 ms (> 5000 steps/cycle); however, other

Downloaded from asmedigitalcollection.asme.org/biomechanical/article-pdf/135/2/021016/6088427/bio_135_2_021016.pdf by Tufts University user on 15 November 2026

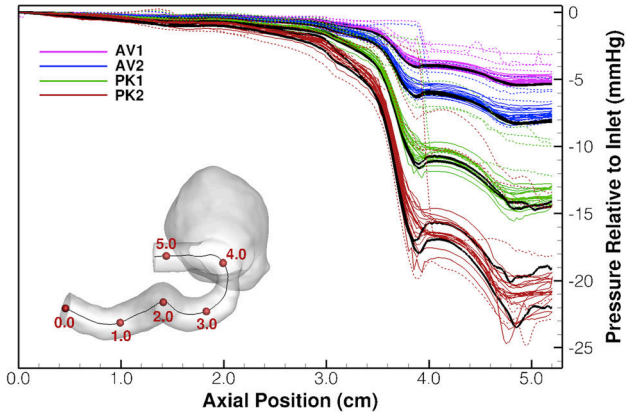


Fig. 8 Phase I centerline pressures for pulsatile flows. Shown are peak systolic (PK1, PK2) and cycle-averaged (AV1, AV2) pressures relative to their respective inlet values. Nominal outliers (E, H, M, N, U) are shown as dotted lines. The two Nektar solutions (W, X) are shown as solid black lines. Inset is the model and centerline, indicating the locations of the axial coordinates.

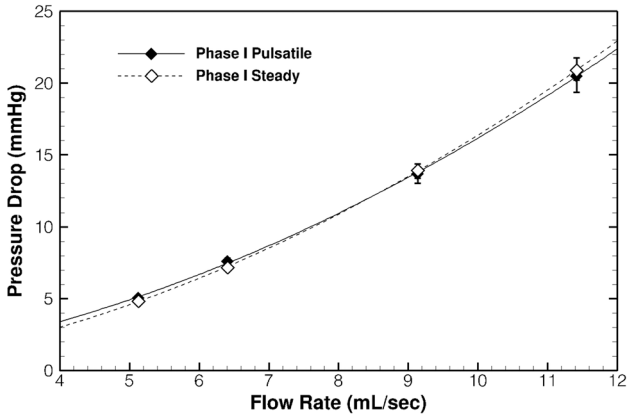


Fig. 9 Inlet-outlet pressure drops versus flow rate for phase I. Included are both pulsatile (AV1, AV2, PK1, PK2) and steady state (SS1, SS2, SS3, SS4) data. Symbols identify the median values; error bars identify the interquartile ranges. Best-fit second-order polynomial curves demonstrate the quadratic nature of the pressure versus flow relationship ($R^2 > 0.999$ in both cases).

solutions with comparably fine time steps reported smoother isosurfaces. It is also worth noting that the outliers identified for the pressure predictions (E, H, M, N, U) showed a variability of flow patterns comparable to that for the rest of the solutions. Figure 11 shows that cycle-averaged (AV2) flow patterns were much more similar across the solutions, and it is notable that solutions with the least amount of inflow penetration during systole did not necessarily show the same behavior for cycle-averaged flow. Similar trends with regard to agreement and outliers were noted for the pulsatile1 case (not shown), with the exception that flow instabilities were not evident for the lower peak systolic flow rate (PK1).

Finally, centerline velocities for pulsatile2 peak systolic and cycle-averaged flow (Fig. 12) revealed fairly large variations in maximum velocity at the stenosis throat (axial position ≈ 3.8 cm) and near the outlet. The effect of the various inlet velocity conditions was evident from the "banding" of velocities at the left side of the plot. Inspection of velocity isocontours revealed that the wide velocity differences along the tortuous parent artery could be attributed to more subtle differences in velocity profile skewing or rotation of the helical flow as it intersected the centerline.

Phase II. Surface maps of peak systolic pressure (Fig. 13) and cycle-averaged pressure (Fig. 14) show somewhat more variability across solutions compared to the corresponding phase I data. It is also worth noting that outlier solutions from phase I were not necessarily outliers in phase II and vice versa. In general, pressures in the aneurysm sac were lower than for phase I, indicating a stronger pressure drop. This is confirmed in Fig. 15, which shows pressure drops nearly 10 mmHg greater than for phase I, although the characteristic behavior of pressure along the centerline was similar.

Figure 16 confirms that the CFD-predicted phase II pressure drops were substantially higher than those for phase I, even after accounting for the 11.3% difference in fluid density. More noteworthy, however, is that the *predicted* phase II pressure drops were even higher than the *measured* ones, nearly double at the lower flow rates and up to 60% at the higher flow rates per Table 3. As discussed below, some of this discrepancy could be attributed to subtle differences between the physical flow model and its reconstruction from micro-CT. Nevertheless, while the CFD data showed a clear quadratic dependence of pressure drop on flow for both pulsatile and steady conditions, such dependence was only evident experimentally for the steady flow conditions.

Table 3 Descriptive statistics for inlet-outlet pressure drops (in mm Hg)

	Phase I CFD	Phase II CFD	Phase II Measured
Case	Median (IQR*)	Median (IQR*)	Mean ± stdev
AV1	5.0 (4.8–5.1)	5.6 (5.2–5.7)	2.31 ± 0.04
AV2	7.6 (7.2–7.8)	10.0 (9.4–10.2)	5.15 ± 0.05
PK1	13.7 (13.0–13.9)	19.3 (17.7–20.3)	16.29 ± 0.74
PK2	20.5 (19.4–21.0)	27.8 (25.6–28.8)	19.18 ± 0.49
SS1	4.8 (4.7–4.9)	6.7 (6.5–6.9)	3.44 ± 0.27
SS2	7.2 (7.0–7.3)	10.0 (9.7–10.1)	5.34 ± 0.24
SS3	13.9 (13.4–14.4)	19.5 (18.6–20.3)	12.25 ± 0.12
SS4	20.9 (20.2–21.8)	29.1 (27.7–30.0)	18.53 ± 0.11

*Interquartile range

Discussion

Main Findings. The primary objective of this study was to determine the *variability* of CFD solutions from a wide range of groups, under quasi-real-world conditions, i.e., provided only with a lumen surface and flow rates but with no guidance for discretization or solution strategy. Although a wide variety of solvers and solution strategies was employed, the resulting pressure drop predictions were remarkably consistent, typically differing by less than 10%. A few outliers were identified, but there were no obvious factors to discriminate those from the other solutions, suggesting the possibility that errors in the postprocessing—nevertheless an integral part of the CFD solution pipeline—could also be to blame. On the other hand, upon closer inspection of the flow details (e.g., pressure recovery, flow patterns), there was a wider variation across the solutions. Moreover, those solutions that were outliers for velocity were not necessarily outliers for pressure and vice versa. Again, however, there was no obvious trend, with respect to solution strategy, with the exception that high temporal resolution (>5000 steps/cycle) appeared to be a necessary (but not sufficient) condition for detecting flow instabilities that were evident at the higher peak systolic flow rate (PK2).

With regard to the secondary objective of this study, the 27 independent and blinded CFD solutions confirmed the presence of a high peak systolic inlet-outlet pressure drop (~20 mmHg) due primarily to the presence of a mild (<50% by diameter) stenosis proximal to the aneurysm sac, albeit about 5 mmHg less than the 25 mmHg reported by Cebral et al. On the other hand, a physiologically plausible 20% reduction in the presumed inlet WSS (i.e.,

Downloaded from asmedigitalcollection.asme.org/biomechanical/article-pdf/135/2/021016/6088427/bio_135_2_021016.pdf by Tufts University user on 15 November 2026

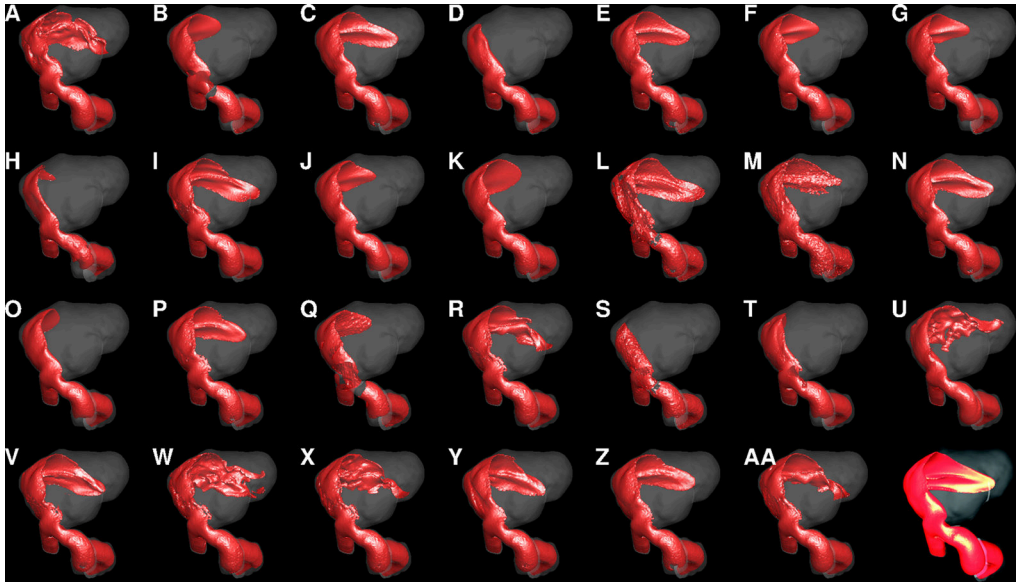


Fig. 10 Phase I, pulsatile2 peak systolic (PK2) velocities. Shown are isosurfaces of velocity magnitude at 50 cm/s. The original panel from Ref. [11] is shown at bottom right.

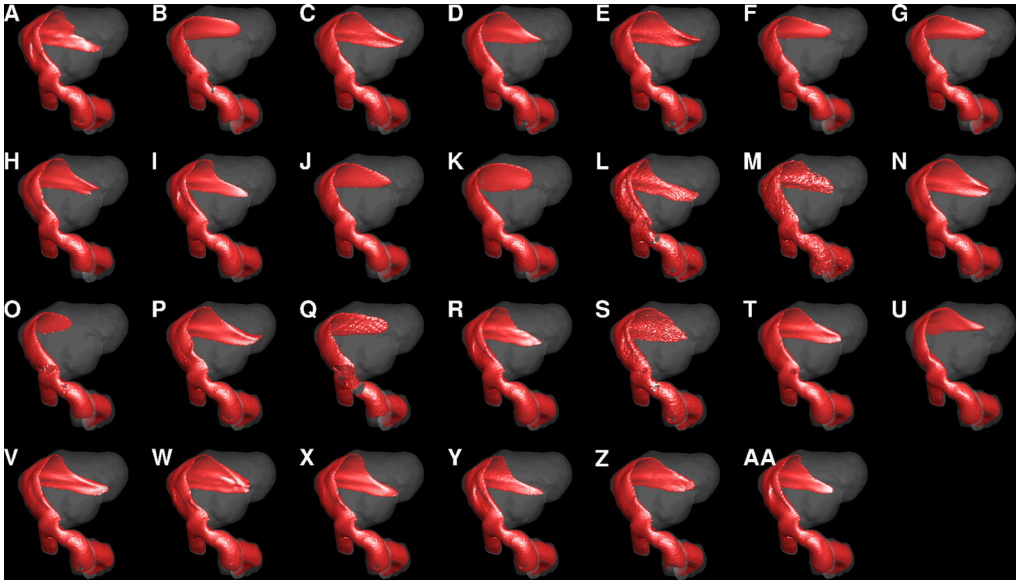


Fig. 11 Phase I, pulsatile2 cycle-average (AV2) velocities. Shown are isosurfaces of velocity magnitude at 30 cm/s.

from 15 dyn/cm^2 to 12 dyn/cm^2) resulted in a marked reduction of the peak systolic pressure drop to 14 mmHg, by virtue of the demonstrated quadratic dependence of pressure drop on flow rate. Taken together, and apropos of the concerns raised by Fiorella et al. [12], the present CFD Challenge verifies that Cebral et al.'s CFD solutions are in the right ballpark [11], at least for their assumed pulsatile flow conditions. However, the findings of the Challenge and the discussion that follows should serve as a reminder of how sensitive the predicted pressure drops can be to the assumed flow rates, particularly in the presence of a stenosis, even one <50% by diameter.

Discrepancy Between Measured and Predicted Pressure Drops. A notable finding was that CFD-predicted pressure drops for phase II were up to 60% higher than those measured experimentally under the same flow conditions. A clue to the possible source of this discrepancy was provided by the fact that the experiments agreed more closely with the phase I pressure drops, even after accounting for the higher fluid density of the phase II versus phase I simulations (Fig. 16). Knowing that that pressure drop is highly dependent on lumen size, we suspected that the flow model's lumen geometry may not have been maintained throughout the fabrication process despite the obvious care taken to avoid this, as described in the Methods. Indeed, this seemed to be the case when comparing phase II versus phase I CFD model cross-sectional areas, as shown in Fig. 17.

To test this, optical coherence tomography (OCT) was performed on the aneurysm model to confirm the micro-CT measurements upon which the phase II CFD model was based. The OCT acquisition was performed at Erasmus Medical Centre in Rotterdam by using commercially available C7-XR OCT Intravascular

Downloaded from asmedigitalcollection.asme.org/biomechanical/article-pdf/135/2/021016/6088427/bio_135_2_021016.pdf by Tufts University user on 15 November 2026

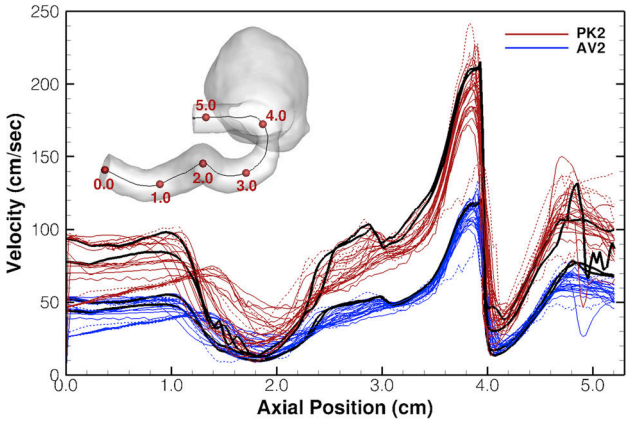


Fig. 12 Phase I centerline velocities for pulsatile2 flow. Shown are peak systolic (PK2) and cycle-averaged (AV2) velocity magnitudes. Nominal outliers from the pressure plots (E, H, M, N, U) are shown as dotted lines. The two Nektar solutions (W, X) are shown as solid black lines.

Imaging System (Lightlab Imaging Inc., Westford, MA) with C7 Dragonfly Imaging Catheter. Images were acquired during an automated pullback rate of 10 mm/s. The distance between image frames was 0.1 mm with an in-plane resolution of 15 μm. The lumen borders of each cross-sectional image were manually delineated by an OCT expert. The geometrical information such as lumen area and mean, minimum, and maximum measured diameters were automatically calculated by the OCT application software package. As also shown in Fig. 17, OCT-measured areas were nearly identical to those of the phase I CFD model, rather than the phase II CFD model or the CT scans upon which it was based. A notable exception is that the minimum stenosis area as measured by OCT was 8.6 mm^2, compared to 7.5 mm^2 for the phase I CFD model, and 6.3 mm^2 for the phase II CFD model (and; consequently, the micro-CT scans).

In light of this surprising discrepancy between micro-CT and OCT, the flow model areas were also measured by intravascular ultrasound (IVUS), also performed at Erasmus MC with a Galaxy 2 System (Boston Specific) using a 30 MHz UltraCross 2.9 Coronary Imaging Catheter. The frame rate of the Galaxy 2 system was 30 frames/s. The distance between image frames in the IVUS system was 0.033 mm. The catheter was automatically pulled back with a speed of 1 mm/s. The lumen delineation was manually done by an IVUS expert. The area and diameter measurements were automatically calculated by the Galaxy 2 System. The difference in the area measurements between OCT and IVUS was approximately 1% at all cross sections, thus verifying the OCT measurements.

In other words, the fabricated flow model reproduced well the dimensions of the nominal phase I geometry as designed, meaning that the micro-CT measurements somehow underestimated the dimensions when constructing the phase II geometry and consistently for two different micro-CT scanners, as shown in Fig. 17. Manual measurement of dimensions from the micro-CT images revealed only a minor sensitivity to the choice of threshold, and so we were left to conclude that the presence of the residual LMPA served to distort the micro-CT acquisitions. Some evidence for this can be seen at the far right of Fig. 17 (axial position $>$ 7 cm), where OCT measurements more closely match those of the Akron micro-CT (the London micro-CT scans did not extend this far). This is a location where the outlet ports were added so as to accommodate the Tygon tubing, which was left attached to the flow model during scanning (i.e., there was no residual LMPA at the lumen/tube interface).

In light of the fact that the experiments had, in retrospect, been carried out on a model closer to the phase I geometry, we invited groups to participate in an optional phase III, in which the phase II flow rates and fluid properties were imposed on the phase I CFD model. As shown in Fig. 18, for the 11 phase III solutions contributed, the median pressure drops were virtually identical to those from the full set of density-corrected phase I solutions. This left a 3–5 mmHg overestimation of pressure drop by the median CFD data, corresponding to $\sim$25% at the peak systolic values. Referring to Fig. 17, however, it should be remembered that even the phase I CFD model had a smaller minimum area (7.5 mm^2) compared to the physical model (8.6 mm^2), suggesting that we could have achieved better agreement between CFD and experiments had we been able to digitally reconstruct the physical model with better accuracy. These differences in minimum stenosis area correspond to only a 0.11 mm difference in minimum radius assuming a circular cross section, and something we might have avoided had we chosen to use a scaled-up physical model. Nevertheless, this should serve as a potent reminder of how sensitive

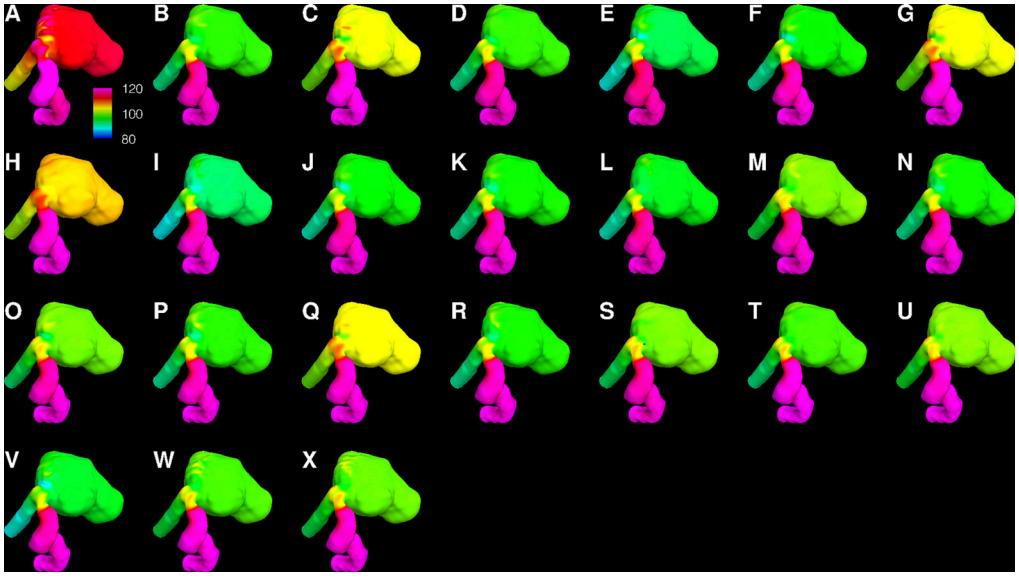


Fig. 13 Surface maps of peak systolic pressures for phase II, pulsatile2 flow (PK2). Letters identify the different contributed solutions, and in all cases are presented with the inlet pressure set to 120 mm Hg and a color scale ranging from 80–120 mm Hg, as shown in panel A.

Downloaded from asmedigitalcollection.asme.org/biomechanical/article-pdf/135/2/021016/6088427/bio_135_2_021016.pdf by Tufts University user on 15 November 2026

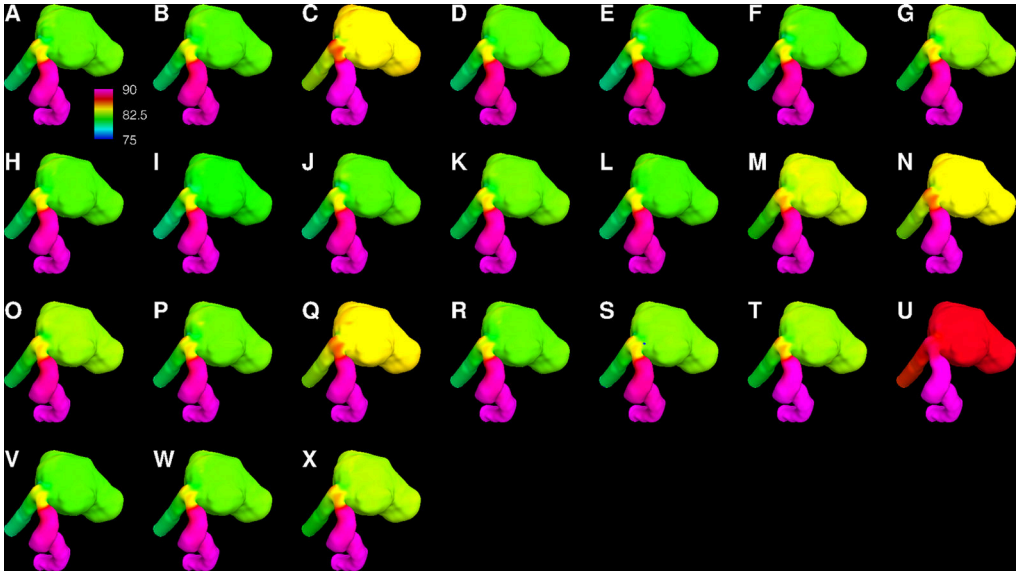


Fig. 14 Surface maps of cycle-averaged pressures for phase II, pulsatile2 flow (AV2). Inlet pressure is assumed to be 90 mm Hg, and the color scale now ranges from 75–90 mm Hg.

pressure drops can be, not only to flow rates as already demonstrated, but also to subtle differences and/or errors in stenosis measurement, whether by micro-CT or *in vivo* imaging. It is also worth noting that, in general, CFD may overestimate or underestimate pressures, depending on the biases in the flow rates and stenosis measurement.

What remains unclear is why the measured peak systolic pressure drop, PK1, does not follow the trends evident from the CFD data and the steady flow measurements as seen in Fig. 18, whereas PK2 does follow this trend. PK1 pressure drops from the three separate acquisitions of nine cycles were 16.02 ± 0.54, 16.83 ± 0.95, and 16.03 ± 0.31 mmHg. Data from the second acquisition was biased upwards because three of the nine cycles experienced peak systolic pressure drops in the range of 17–18 mmHg, whereas the other six cycles were within 15.5–16.5 mmHg, comparable to ranges from the first and third acquisitions. These seemingly consistent measurements are, however, still well above the ~12 mmHg that would be expected if the quasi-steady assumption holds, as it seems to for the CFD models. If we accept the measured PK1 pressure drop data at face value, this would imply that the quasi-steady assumption does not hold for peak systolic conditions. However, this seems unlikely given that the higher PK2 pressure drop followed this quasi-steady assumption rather closely. Furthermore, inspection of the entire pulsatile2 pressure drop waveform from both measurements and selected CFD solutions showed that the quasi-steady assumption holds throughout the cardiac cycle. This was also true for the pulsatile1 pressure drop waveform, except for a short time period (~30 ms) around peak systole, i.e., PK1. This is surprising given that the two measured flow waveforms are similar with regard to systolic acceleration and deceleration (c.f., Fig. 4). One possible explanation is that the flow system had sufficient compliance to cause the flow probe, positioned 30 cm upstream of the model, to report a different peak systolic flow rate than that which was actually experienced by the flow model downstream, where the pressures were measured. Although compliance of the tubing was minimal for this system, the pulsatile1 case required a

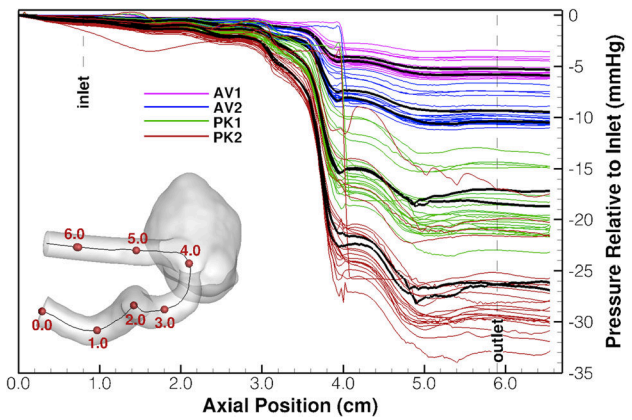


Fig. 15 Phase II centerline pressures, relative to CFD model inlet pressure. As before the two Nektar solutions (W, X) are shown as solid black lines; however, outliers are not highlighted by dotted lines. Inset is the model and centerline, indicating the locations of the axial coordinates. Also shown are the locations where inlet and outlet pressure were measured experimentally.

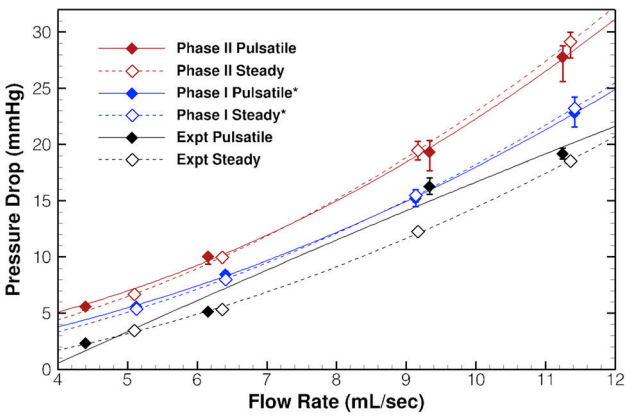


Fig. 16 Phase II pressure drop versus flow rate. As in Fig. 9, both pulsatile and steady pressures are included, and phase I and phase II data are shown as the median and interquartile ranges. Experimental data are shown as means ± standard deviation based on three repeat runs for the pulsatile flows and six measurements for the steady flows. As indicated by the asterisk in the legend, phase I pressures have been scaled by a factor of 1.113 to account for the higher fluid density used for the phase II simulations and experiments. Best-fit second-order polynomial curves demonstrate the quadratic nature of the pressure drop versus flow relationship ($R^2 > 0.999$ except for Expt Pulsatile, $R^2 = 0.98$).

Downloaded from asmedigitalcollection.asme.org/biomechanical/article-pdf/135/2/021016/6088427/bio_135_2_021016.pdf by Tufts University user on 15 November 2026

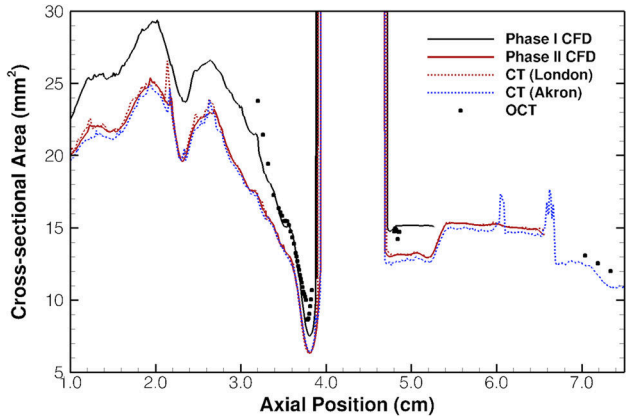


Fig. 17 Cross-sectional areas of the two CFD models versus those from CT and OCT scans of the flow model. Note that the phase II CFD model and CT (London) area essentially overlap since the former was based on (volume-preserving) smoothing of the latter.

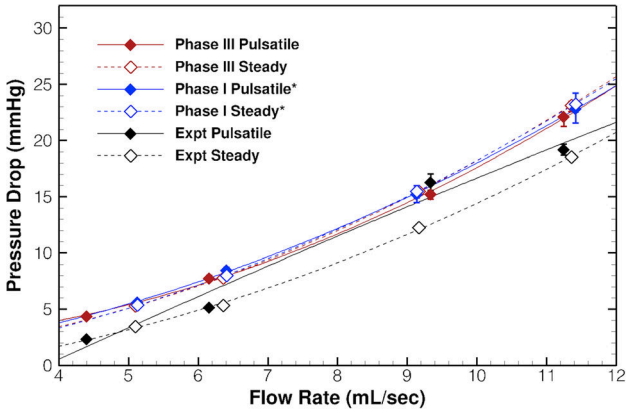


Fig. 18 Phase III pressure drop versus flow rate, compared to phase I and experiments. See caption of Fig. 16 for further explanation of plot elements.

lower pumping pressure than pulsatile2, and, thus, the pulsatile1 flow waveform might have been more susceptible to alterations due to rapid fluid deceleration and acceleration during systole. We may, therefore, speculate that the experimental and CFD flow rates were more consistent for the pulsatile2 case, and thus, the PK2 data followed the trends of the CFD data and steady flow measurements.

Limitations and Perspectives. As noted in the Introduction, a conscious decision was made not to test or comment on Cebral et al.'s clinical hypothesis nor to prove whether their flow rates were appropriate or not for this case. We also took Cebral et al.'s geometry at face value, rather than add further uncertainty to the process by asking participants to segment the original images. Thus, we are in no position to confirm or refute the "truth" of the reported pressure drops but rather can only state with some confidence that they are broadly consistent with what is expected given the geometry and the assumed flow rates. It should also be remembered that this was not a scientific sampling of research groups, CFD solvers, or solution strategies but rather a response to an open call. Having said this, many of the participating groups likely would describe themselves as experts in cardiovascular CFD. Furthermore, consider that solutions F and V, contributed by groups well-published in CFD modeling of cerebral aneurysms, reported phase I PK2 pressure drops of 19.7 mmHg and 22.3 mmHg. Similarly, solutions W and X, contributed by two well-known CFD groups using the same spectral element solver, report phase I PK2 pressure drops of 19.1 mmHg and 22.0 mmHg. These ranges are greater than the corresponding IQR of 1.6 mmHg shown in Table 3, and so the IQR values reported in our study are probably conservative estimates of the variability of published solutions in the literature.

We also did not attempt to separate CFD solution errors from possible errors due to postprocessing of the data since, in the end, we were attempting to reproduce a complete quasi-clinical workflow. Unfortunately, it was also not possible, given the design of this study, to provide concrete recommendations for solution strategies that would result in an adequately resolved solution since this depends on many factors. What we can say, and perhaps this is (or should be) obvious, is that variability of the solutions did not appear to depend on the choice of solver but rather on the solution strategy and discretization. One concrete finding, however, was the detection of flow instabilities almost certainly present at peak systolic flow for the pulsatile2 case (PK2) required high temporal resolution with 5000 or more time steps per cycle.

A conscious decision was also made not to quantify variability for velocities or investigate WSS. It remains unclear which hemodynamic factors or quantitative metrics are clinically relevant [21,22], and so it is possible that, say, WSS uncertainties would appear higher than the usual tolerances that engineers are used to, but which would not change a particular case's stratification for rupture risk or treatment decision. In this regard, future challenges aimed at investigating quantities like WSS may wish to focus not on a fine-grained analysis of uncertainties for a single case but rather whether different groups would rank-order cases differently based on some presumed clinical risk according to one or more agreed-upon hemodynamic criteria. An additional wrinkle, to make this especially challenging but also more clinically relevant, would be to provide only the geometry and let participants choose the flow rates and/or provide only the images and let participants extract the geometry. It would also be worth investigating how variability due to CFD solver and/or solution strategy compares to the well-studied effects of modeling assumptions (e.g., rigid walls, Newtonian viscosity, fully developed inflow) and geometry reconstruction errors or uncertainties.

In the end we hope this Challenge will inspire others to lead future challenges and will also serve as a benchmark for others to test their solvers or solution strategies. Towards this end, the CFD Challenge instructions and contributed data are available online[2].

Conclusions

In summary, this inaugural CFD Challenge has demonstrated a remarkable concordance of pressure drop predictions for a nontrivial, anatomically realistic case across a wide variety of CFD solvers and solution strategies. Qualitatively, there was higher variability in the flow patterns, notably the penetration of high-speed flow into the aneurysm sac. The practical significance of these velocity differences is not clear and could be the subject of future CFD Challenges. A quasi-steady assumption was found to have negligible impact on the CFD-predicted pressures. Together with simulations at two different pulsatile flow rates, these confirmed an expected nonlinear dependence of pressure drop on flow rates, which highlighted the sensitivity of predicted pressure drops to assumptions about the flow rate and to uncertainties in the dimensions of a mild stenosis.

Acknowledgment

The authors would like to thank Juan Cebral for agreeing to be the "subject" of this study and for providing the lumen geometry and flow rate data. We also thank David Holdsworth for providing access to micro-CT facilities at the Robarts Research Institute,

[2]http://www.mie.utoronto.ca/labs/bsl/SBC2012cfdchallenge

Downloaded from asmedigitalcollection.asme.org/biomechanical/article-pdf/135/2/021016/6088427/bio_135_2_021016.pdf by Tufts University user on 15 November 2026

Sharon Usip at the Northeast Ohio Medical University, and Merih Cibis and Frank Gijsen for undertaking the OCT and IVUS scans. Authors DAS and FL would also like to thank all of the Challenge participants for their efforts and enthusiastic participation. DAS would like to acknowledge the financial support of Canadian Institutes of Health Research operating grant MOP-62934 and a Heart & Stroke Foundation Career Investigator award. Facilities used for the Phase II experiments were supported by grants from Enterprise Ireland, Applied Research Enhancement (ARE), 2005, CRS/2008/GM02; the Department of Education Ireland, Strand III, 2008, RE20059; and the Irish Research Council for Science, Engineering and Technology.

References

[1] Taylor, C. A., and Steinman, D. A., 2010, "Image-Based Modeling of Blood Flow and Vessel Wall Dynamics: Applications, Methods and Future Directions," Ann. Biomed. Eng., **38**(3), pp. 1188–1203.

[2] Steinman, D. A., 2011, "Assumptions in Modelling of Large Artery Hemodynamics," Ambrosi, D., Quarteroni, A., and Rozza, G. (eds.), *Modelling of Physiological Flows*, Springer-Verlag, Milan.

[3] Ford, M. D. Nikolov, H. N., Milner, J. S., Lownie, S. P., Demont, E. M., Kalata, W., Loth, F., Holdsworth, D. W., and Steinman, D. A., 2008, "PIV-Measured Versus CFD-Predicted Flow Dynamics in Anatomically Realistic Cerebral Aneurysm Models," ASME J. Biomech. Eng., **130**(2), p. 021015.

[4] Raschi, M., Mut, F., Byrne, G., Putman, C. M., Tateshima, S., Vinuela, F., Tanoue, T., Tanishita, K., and Cebral, J. R., 2012, "CFD and PIV Analysis of Hemodynamics in a Growing Intracranial Aneurysm," Int. J. Num. Meth. Biomed. Eng., **28**(2), pp. 214–228.

[5] van Ooij, P., Guedon, A., Poelma, C., Schneiders, J., Rutten, M. C., Marquering, H. A., Majoie, C. B., VanBavel, E., and Nederveen, A. J., 2012, "Complex Flow Patterns in a Real-Size Intracranial Aneurysm Phantom: Phase Contrast MRI Compared With Particle Image Velocimetry and Computational Fluid Dynamics," NMR Biomed., **25**(1), pp. 14–26.

[6] Rayz, V. L., Boussel, L., Acevedo-Bolton, G., Martin, A. J., Young, W. L., Lawton, M. T., Higashida, R., and Saloner, D., 2008, "Numerical Simulations of Flow in Cerebral Aneurysms: Comparison of CFD Results and *In Vivo* MRI Measurements," ASME J. Biomech. Eng., **130**(5), p. 051011.

[7] Arzani, A., Dyverfeldt, P., Ebbers, T., Shadden, S. C., 2012, "*In Vivo* Validation of Numerical Prediction for Turbulence Intensity in an Aortic Coarctation," Ann. Biomed. Eng., **40**(4), pp. 860–870.

[8] Sun, Q., Groth, A., and Aach, T., 2012, "Comprehensive Validation of Computational Fluid Dynamics Simulations of *In-Vivo* Blood Flow in Patient-Specific Cerebral Aneurysms," Med. Phys., **39**(2), pp. 742–754.

[9] Radaelli, A. G., Augsburger, L., Cebral, J. R., Ohta, M., Rufenacht, D. A., Balossino, R., Benndorf, G., Hose, D. R., Marzo, A., Metcalfe, R., Mortier, P., Mut, F., Reymond, P., Socci, L., Verhegghe, B., and Frangi, A. F., 2008, "Reproducibility of Haemodynamical Simulations in a Subject-Specific Stented Aneurysm Model—a Report on the Virtual Intracranial Stenting Challenge 2007," J. Biomech., **41**(10), pp. 2069–2081.

[10] Stewart, S. F. C., Paterson, E. G., Burgreen, G. W., Hariharan, P., Giarra, M., Reddy, V., Day, S. W., Manning, K. B., Deutsch, S., Berman, M. R., Myers, M. R., and Malinauskas, R. A., 2012, "Assessment of CFD Performance in Simulations of an Idealized Medical Device: Results of the FDA's First Computational Interlaboratory Study," Cardiovasc. Eng. Technol., **3**(2), pp. 139–160.

[11] Cebral, J. R., Mut, F., Raschi, M., Scrivano, E., Ceratto, R., Lylyk, P., and Putman, C. M., 2011, "Aneurysm Rupture Following Treatment With Flow-Diverting Stents: Computational Hemodynamics Analysis of Treatment," AJNR Am. J. Neuroradiol., **32**(1), pp. 27–33.

[12] Fiorella, D., Sadasivan, C., Woo, H. H., and Lieber, B., 2011, "Regarding 'Aneurysm rupture following treatment With flow-diverting stents: computational hemodynamics analysis of treatment,'" AJNR Am. J. Neuroradiol., **32**(5), pp. E95–E97; author reply E98–E100.

[13] Yim, P. J., Cebral, J. R., Weaver, A., Lutz, R. J., Soto, O., Vasbinder, G. B., Ho, V. B., and Choyke, P.L., 2004, "Estimation of the Differential Pressure at Renal Artery Stenoses," Magn. Reson. Med., **51**(5), pp. 969–977.

[14] Steinman, D. A., 2011, "Computational Modeling and Flow Diverters: A Teaching Moment," AJNR Am. J. Neuroradiol. **32**(6), pp. 981–983.

[15] Antiga, L., Piccinelli, M., Botti, L., Ene-Iordache, B., Remuzzi, A., Steinman, D. A., 2008, "An Image-Based Modeling Framework for Patient-Specific Computational Hemodynamics," Med. Biol. Eng. Comput., **46**(11), pp. 1097–1112.

[16] Cheng, C., Helderman, F., Tempel, D., Segers, D., Hierck, B., Poelmann, R., van Tol, A., Duncker, D. J., Robbers-Visser, D., Ursem, N. T. C., van Haperen, R., Wentzel, J. J., Gijsen, F., van der Steen, A. F. W., de Crom, R., Krams, R. 2007, "Large Variations in Absolute Wall Shear Stress Levels Within One Species and Between Species," Atherosclerosis, **195**(2), pp. 225–235.

[17] Morris, L., O'Donnell, P., Delassus, P., and McGloughlin, T., 2004, "Experimental Assessment of Stress Patterns in Abdominal Aortic Aneurysms Using the Photoelastic Method," Strain **40**(4), pp. 165–172.

[18] O'Brien, T., Morris, L., O'Donnell, M., Walsh, M., and McGloughlin, T., 2005, "Injection-Moulded Models of Major and Minor Arteries: The Variability of Model Wall Thickness Owing to Casting Technique," Proc. Inst. Mech. Eng. H, **219**(H5), pp. 381–386.

[19] Ene, F., Gachon, C., Delassus, P., Carroll, R., Stefanov, F., O'Flynn, P., and Morris, L., 2011, "*In Vitro* Evaluation of the Effects of Intraluminal Thrombus on Abdominal Aortic Aneurysm Wall Dynamics," Med. Eng. Phys., **33**(8), pp. 957–966.

[20] Fahy, P., Delassus, P., O'Flynn, P., and Morris, L., 2011, "An Experimental Study of the Effects Anatomical Variations Have on Collateral Flows Within the Circle of Willis," Proc ASME Summer Bioeng. Conf., Farmington, VA, June 2011.

[21] Kallmes, D. F., 2012, "Point: CFD—Computational Fluid Dynamics or Confounding Factor Dissemination," AJNR Am. J. Neuroradiol., **33**(3), pp. 395–396.

[22] Cebral, J. R., and Meng, H., 2012, "Counterpoint: Realizing the Clinical Utility of Computational Fluid Dynamics—Closing the Gap," AJNR Am. J. Neuroradiol., **33**(3), pp. 396–398.

Downloaded from asmedigitalcollection.asme.org/biomechanical/article-pdf/135/2/021016/6088427/bio_135_2_021016.pdf by Tufts University user on 15 November 2026